Contemporary and historical detection of small lakes using cross-sensor super resolution Landsat imagery

Ethan D. Kyzivat[a]* (twitter: @EthanKyzivat), Laurence C. Smith[a]

[a] Department of Earth, Environmental & Planetary Sciences and Institute at Brown for Environment & Society, Brown University, 85 Waterman St., Providence, RI 02912, USA (e-mail: *ethan_kyzivat@brown.edu).

Non peer-reviewed pre-print manuscript submitted to *International Journal of Applied Earth Observation & Geoinformation (JAG)*

Manuscript submitted to Int. J. of Applied Earth Observation & Geoinformation (JAG)

Contemporary and historical detection of small lakes using cross-sensor super resolution Landsat imagery

Ethan D. Kyzivat[a]*, Laurence C. Smith[a]

Abstract—Landsat is the longest-running environmental satellite program and has been used for surface water mapping of large water bodies since its launch in 1972. Remote sensing image resolution is increasingly being enhanced through single image super resolution (SR), a machine learning task typically performed by neural networks. Here, we show that a 10x SR model (Enhanced Super Resolution GAN, or ESRGAN) trained entirely with Planet SmallSat imagery (3 m resolution) can be applied to 30 m Landsat imagery to produce 3 m Landsat SR images with preserved radiometric properties. We test the utility of these Landsat SR images for small lake detection by applying a simple water classification to SR and native Landsat imagery and comparing to independent, high-resolution water maps. SR images appear realistic and have fewer missed detections (type II error) compared to LR, but exhibit errors in lake location and shape, and yield increasing false detections (type I error) with decreasing lake size. SR enhancement improves detection of small lakes sized several Landsat pixels or less, with a minimum mapping unit (MMU) of ~ $^{2}/_{3}$ of a Landsat pixel. We also apply the SR model to a historical Landsat 5 image and find similar performance gains, using an independent 1985 air photo map of 242 small Alaskan lakes. This demonstration of retroactively generated 3 m imagery dating to 1985 has exciting applications beyond water detection. Yet, much work remains to be done surrounding technical and ethical guidelines for the creation, use, and dissemination of SR satellite imagery.

Keywords: SISR; SRM; size distribution; object detection; upscaling; downscaling

1. Introduction

LANDSAT, the world's longest-running environmental satellite program, began in 1972 and has retained 30 m spatial resolution since 1982 (Wulder et al. 2019). Landsat 5, 7, 8, and 9 satellites operated by NASA and the United States Geological Survey (USGS) have continuously collected 30 m data through three decades of operation, creating the world's longest archive of satellite data from a single program. Since 2008, the existing archive and all future data were made available for free (Woodcock et al. 2008), also making the Landsat program the first to offer such a huge global image inventory without restriction or cost (Wulder et al., 2016). NASA and the USGS have a directive to continue the Landsat program through future satellite launches, further adding to its > 7.5 million image archive (Wulder et al. 2016). Thus, the Landsat program is unprecedented in its longevity, availability, and continuity.

Landsat has been used for surface hydrology for decades (Smith 1997), but its 30 m resolution makes detecting small lakes and narrow rivers challenging (Yang et al. 2019; Allen et al. 2018). This is a significant impediment to obtaining accurate lake inventories because lake-size distributions (LSDs, Downing et al. 2006) commonly follow power law distributions, making small lakes far more abundant than large ones, although there are exceptions (Muster et al. 2019). Power law behavior can only be modeled for lakes > 0.3-

[a] Department of Earth, Environmental & Planetary Sciences and Institute at Brown for Environment & Society, Brown University, 85 Waterman St., Providence, RI 02912, USA (e-mail: ethan_kyzivat@brown.edu). *Corresponding author. Abbreviations: SR=super resolution; LR=low resolution; GT=ground truth; GAN=generative-adversarial network; ESRGAN= Enhanced Super Resolution Generative-Adversarial Network; CNN=convolutional neural network; MMU=minimum mapping unit; AP=average precision; AR=average recall; AF1=average F-1 score; LSD=lake-size distribution; TP=true positive; FP=false positive; FN=false negative; ABoVE=Arctic-Boreal Vulnerability Experiment GSW= Global Surface Water

0.46 km^2 (Kyzivat et al. 2019b; Cael and Seekell 2016), so small lakes below this limit are therefore the most abundant but hardest to estimate by extrapolation. For this reason, improving the detection limit to ever-smaller lake sizes is an ongoing goal for hydrologic studies (Paltan et al. 2015; Verpoorter et al. 2014; Messager et al. 2016; Kyzivat et al. 2019b; Muster et al. 2019).

Individual pixels are not sufficient to detect lakes or their distributions, and must instead be grouped into objects. Raster map products like the Global Surface Water (GSW) suite (Pekel et al. 2016) use a minimum mapping unit (MMU) of one Landsat pixel, but a single water pixel is not guaranteed to be a lake. Vector classifications, which delineate discrete water bodies as objects typically have an MMU of several pixels, such as 40 pixels (40 m^2) for airborne camera imagery (Kyzivat et al. 2019b; Muster et al 2019); 10 pixels (1,000 m^2 or 0.001 km^2) for Sentinel-2 (Sui et al. 2022); 9 pixels (0.002 km^2) for pansharpened Landsat 7 (Verpoorter et al. 2014); 4 pixels (0.0036 km^2) for Landsat 8 (Paltan et al. 2015); and 33 pixels (0.03 km^2) for combined Landsat (Pi et al. 2022) imagery. While convention requires an MMU of 4-33 Landsat pixels (3,600 – 8,100 m^2), such limits, in practice, still undercount small lakes, with high-resolution mapping showing that 70% of sampled northern lakes are smaller than 4 pixels and would thus be excluded (Kyzivat et al. 2018, 2019a).

These MMU selections follow a trend where fewer pixels are required for a confident lake detection as spatial resolution becomes coarser. A 1 km^2 pixel detection is unlikely to be false, for example, whereas a 500 m^2 pixel detection is more likely to be a lake, river fragment, cloud shadow, or terrain shadow. Therefore, vector-based classifications are preferable for quantifying lake-size distributions, particularly for lakes sized near the native pixel resolution.

Single image super resolution (SR) is an emerging machine learning tool for enhancing the pixel resolution of images and is increasingly being applied to remote sensing imagery. Among the different SR models, generative-adversarial networks (GANs) produce results with greater perceptual quality and appear crisper to human observers than results from convolutional neural networks (CNNs, Wang et al. 2022). All supervised SR models, such as the one used here, require paired training images at different pixel resolutions. The ratio between these resolutions determines the output resolution and therefore the degree of SR enhancement. Remote sensing SR imagery has been used to enhance object detection, using resolution ratios varying from 2-8x, to detect objects several native resolution (hereafter: low resolution or LR) pixels in size. Shermeyer et al. (2018) produce 2x, 4x and 8x SR resampling ratios from 30 cm LR Worldview-3 imagery, which increases object detection average precision (AP) performance by ~ -2 to 11 percentage points. Rabbi et al. (2020) use a 4x SR ESRGAN-based model on 30 cm and 1.2 m LR airborne imagery to detect cars (5 m length) and oil tanks (3 m diameter) with AP ranging from 77 to 95%. Courtrai et al. (2020) use 8x SR to reconstruct realistic-looking and automatically-detectable cars from just eight 1 m LR airborne and multi-source satellite pixels, with AP of 55 to 77%. Notably, previous SR object detection efforts focus on objects of uniform size still resolvable in LR imagery (e.g. vehicles and oil tanks). They have limited application to broad-scale remote sensing because they delineate only object bounding boxes, rather than counts or sizes; primarily use resampling ratios of <= 8x (Wang et al. 2022); and evaluate results on small image tiles, rather than mosaicked imagery. In sum, there is an opportunity to evaluate the detection of non-uniform sized objects as small as sub-pixels in remote sensing SR imagery, particularly at resolution ratios > 8x, through landscape-scale metrics.

SR model training typically uses LR images derived from resampled (i.e. degraded) high resolution (HR) images (Sustika et al. 2020; Lezine et al. 2021; Wang et al. 2018). Examples include use of HR training data sets such as DIV2K (Agustsson and Timofte 2017; Ignatov et al. 2019) and UC Merced (Yang and Newsam 2010) image datasets. New methods are also emerging to use utilize training images from other sensors with finer resolution, for example training Sentinel-2 imagery with Planet or Worldview imagery (Salgueiro Romero et al. 2020; Galar et al. 2020; Yoo et al. 2021). Such cross-sensor training enables derivation of SR imagery from LR imagery possessing greater radiometric, spectral, and/or global observation frequency of the LR satellite. Previous 5x GAN (Salgueiro Romero et al. 2020) and 2x/4x CNN (Galar et al. 2020) studies trained SR models on paired LR Sentinel-2 and either Planet or Worldview HR images. To avoid learning a faulty SR transformation, they ensured precise image temporal and spatial alignment between training pairs, applying restrictive cloud filtering and image correlation thresholds. To date, cross-sensor studies have trained LR imagery only from Sentinel-2 (Salgueiro Romero et al. 2020; Galar et al. 2020; Yoo et al. 2021) not Landsat, and none demonstrate that their model can be applied to an independent sensor. A remote sensing SR model trained on HR and LR pairs from one sensor and evaluated against images from another would eliminate the labor of producing cross-sensor image pairs, but to our knowledge, none has been demonstrated.

We previously trained the SR GAN-based model ESRGAN on 289 global Planet HR image scenes, using 10x resampled HR images as the paired LR dataset (Lezine et al. 2022). The SR model was prone to artifacts, including realistic-looking, but spurious features (Wang et al. 2022; Lezine et al. 2022). Even so, for Landsat-observable water bodies, the 10x SR model had similar high accuracy to a classification based on conventional, cubic-resampled imagery (Cohen's kappa > 0.97), and outperformed it with the detection of fine-scale shorelines. Remaining questions surrounding the utility of this model include its use for small lake, rather than shoreline, detection; proper interpretation of synthetic images, and its applicability to non-Planet LR input images, including from historical Landsat archives. Considering that GANs were originally developed to create fake imagery (Goodfellow 2014), spurious features raise ethical concerns (Zhao et al. 2021) when being used to interpret and make decisions from SR imagery. To address these questions, we propose a MMU for 10x SR imagery that represents a reliable size threshold to use for object detection.

Here we use our 10x SR model previously trained from Planet images only (Lezine et al. 2021) to test whether a Planet-trained SR model can be used to detect small and sub-pixel lakes in Landsat imagery. We rely on object-, rather than pixel-based metrics to determine how well Landsat SR and LR lake detections agree with the number, size and location of 25,523 Canadian and Alaskan lakes mapped from traditional airborne camera photography (Kyzivat et al., 2018; 2019a; Walter Anthony and Lindgren 2021, Walter Anthony et al. 2021). First, we apply our Planet-trained model to Landsat LR imagery, and test for any unwanted transformation to the image radiometric values in the SR results. Next, we run the same threshold-based water classifier on both LR and SR Landsat imagery. Then, we evaluate the classifier against the independent airborne datasets using novel object-based and spatial metrics designed for remote sensing image mosaics. Finally, we demonstrate retroactive generation of SR imagery from a 1985 Landsat scene. We conclude with some recommendations for developing Landsat SR models, including an appropriate MMU for lake detection, and a caution on the ethical considerations raised by retroactive creation of SR imagery.

2. Data and methods

2.1 Airborne and Landsat remote sensing imagery

A study domain from the NASA Arctic-Boreal Vulnerability Experiment (ABoVE, Miller et al. 2019) was chosen based on the availability of high resolution, lake vector datasets to be used for independent verification of Landsat LR and SR lake detections. Kyzivat et al. (2019a, 2019b) provide a 1 m resolution color-infrared camera orthomosaic, a water mask, and a vectorized lake map acquired concurrently with AirSWOT Ka-band radar data, a prototype of the forthcoming Surface Water and Ocean Topography (SWOT) satellite mission (Fayne et al. 2020). The lake map has a 40 m^2 (40 pixels) native MMU and a maximum lake size of 15.5 km^2. Classification errors in the precursor water mask are largely due to roads, agricultural fields, and clouds/haze, with the latter impacting 28% of the camera product's image tiles. The water mask has a user's accuracy (precision) of 87.1%, and a producer's accuracy (recall) of 94.0%. Image tiles with the fewest clouds were used to create the vector mask, which has a geolocation error of <= 14.7 m RMSE relative to a Digital Globe base map for 90% of the dataset (Kyzivat et al. 2019b). From 23,280 km^2 of camera imagery acquired over 13 regions for the 2017 ABoVE AirSWOT flights, we selected portions of 10 lake-rich regions encompassing 23,212 km^2 to use for SR lake detection (**Figure 1**; **Table 1**). All image processing was carried out in Python 3.9, using the open-source packages *numpy* (Harris et al. 2020), *scipy* (Virtanen et al. 2020), *sckikit-learn* (Pedregosa et al. 2011), *gdal* (GDAL/OGR contributors 2022), *rasterio* (Gillies 2019), and *geopandas* (Jordahl et al. 2020). To comply with previous convention (Wang et al. 2018; Rabbi et al. 2020) we refer to this selected, high-resolution lake map as a "ground truth" (GT) dataset, even though the AirSWOT camera is an airborne sensor.

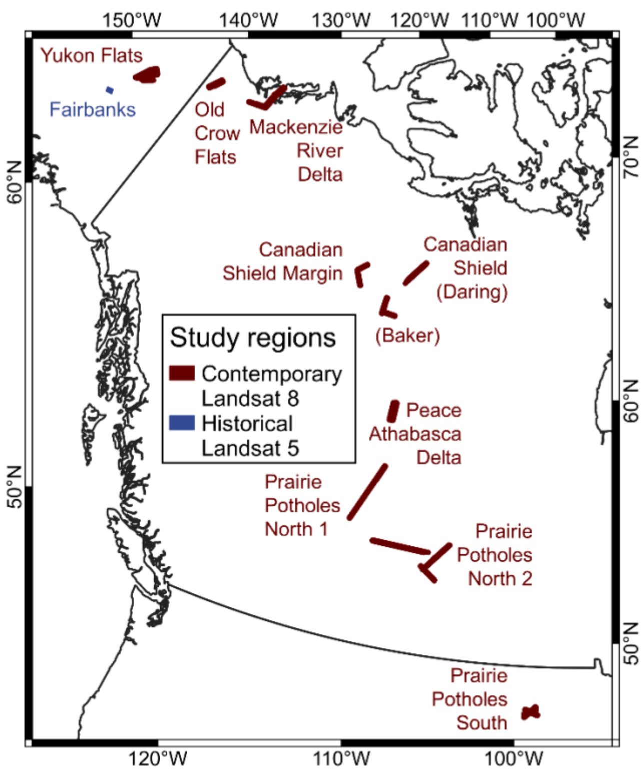

Figure 1. Study regions are derived from available high-resolution vector lake maps created for the NASA Arctic-Boreal Vulnerability Experiment (ABoVE) (Kyzivat et al. 2018; 2019b; in red); and a historical study of permafrost lake change (Walter Anthony et al. 2021, in blue).

15 Landsat 8 scenes were downloaded as Collection 2, level 2 (surface reflectance) products over the identified regions (**Figure 1**). Scenes were selected based on the closest temporal acquisition to the 2017 AirSWOT flights (3-27 days) with < 5% cloud coverage. All scenes were classified as Tier 1, signifying the best available geolocation error of <= 12 m RMSE. In preparation for SR processing, scenes were converted from 16-bit to 8-bit integers, using an image stretch based on the 1- and 95- percentiles of cloud-free pixels to emphasize radiometric contrast between land and water. Finally, scenes were mosaicked (if necessary) and cropped to 48-pixel square tiles with 16 pixels overlap within buffered outlines of the 10 study regions (**Table 1**).

2.2 Lake detection in super and native resolution Landsat imagery

Landsat SR imagery was derived from the Landsat native resolution (i.e. LR) image tiles using the Planet-trained ESRGAN 10x SR model of Lezine et al. (2020), which operates on near-infrared (NIR), green (G) and red (R) 3-band images. This model was first trained on HR images from the DIV2K dataset (Agustsson and Timofte 2017; Ignatov et al. 2019) and then on ~183,000 48-pixel square tiles from 289 Planet scenes (Wang et al. 2018, Lezine et al. 2021), using paired training LR images derived via bicubic resampling. The accuracy of this model was previously assessed at 27.36 peak signal-to-noise ratio (PSNR) compared to 35.06 for a 4x model (Lezine et al. 2021). When applied to Landsat, the model produced SR tiles of dimension 480x480 pixels, corresponding to a 3 m ground sample distance per pixel (commensurate with 3 m resolution Planet imagery). To reconstruct SR versions of the cropped Landsat scenes, output SR tiles were mosaicked using a radial Gaussian weighting function that blended values from multiple tiles in overlapping tile edges. Trial and error showed that a 30-pixel Gaussian standard deviation yielded the smoothest transition between tiles.

Reconstructed Landsat SR scenes were evaluated for radiometric consistency using several statistical tests. First, for visual inspection, image histograms for each band of corresponding LR and SR Landsat scenes were plotted. Next, a Kolmogorov–Smirnov test was used to compare corresponding distributions. Finally, mean band values for LR and SR were calculated over each image and used for the Wilcoxon signed-rank test, a nonparametric comparison between population means that assumes no underlying distribution.

To classify surface water in both SR and LR Landsat images, near-infrared band thresholds for each scene were chosen based on visual analysis following Yamano et al. (2006). This one-parameter (band threshold) method, implemented in ENVI 5.6.1, was chosen for its simplicity, which permits comparison between image resolutions, not classifiers. Only the LR images were used to choose thresholds (**Table 1**), which were verified on corresponding SR images by confirming that the segmentation delineated a reasonable number of lakes without fragmentation near their shorelines (examples of unavoidable fragmentation caused by shadows are in **Figure 3d** and **e**). In sum, the classifier enables verification and modification of thresholds, if needed, and it can be exactly replicated on images of different spatial resolutions, which is crucial for further statistical comparisons.

Table 1. Selected Landsat scenes and near-infrared water classification thresholds (T).

Region	**Landsat ID**	**Year**	**Area (km^2)**	**T**	**Longitude**	**Latitude**
Yukon Flats Basin	LC08_L2SP_068014_20170708_20200903_02_T1	2017	5,141	100	-145.6979	66.4965
	LC08_L2SP_068013_20170708_20201015_02_T1					
Old Crow Flats	LC08_L2SP_067012_20170903_20200903_02_T1	2017	948	50	-139.7607	67.9617
Mackenzie River Delta	LC08_L2SP_064011_20170728_20200903_02_T1	2017	2,275	50	-133.8404	68.6863
	LC08_L2SP_064012_20170728_20200903_02_T1					
Canadian Shield Margin	LC08_L2SP_050015_20170811_20200903_02_T1	2017	1,202	85	-117.4681	63.8111
	LC08_L2SP_048016_20170829_20200903_02_T1					
Canadian Shield	LC08_L2SP_046016_20170831_20200903_02_T1	2017	1,687	83	-114.1445	62.7106

near Baker Creek						
Canadian Shield near Daring Lake	LC08_L2SP_045015_20170723_20201015_02_T1	2017	1,689	100	-112.2817	64.4434
Peace-Athabasca Delta	LC08_L2SP_043019_20170810_20200903_02_T1	2017	2,616	80	-111.4176	58.7111
Prairie Potholes North 1	LC08_L2SP_041021_20170812_20200903_02_T1 LC08_L2SP_041022_20170812_20200903_02_T1	2017	3,076	55	-111.8893	55.2447
Prairie Potholes North 2	LC08_L2SP_038023_20170823_20200903_02_T1	2017	2,892	65	-106.2871	52.901
Prairie Potholes South	LC08_L2SP_031027_20170907_20200903_02_T1	2017	1,688	60	-99.0807	47.0912
Fairbanks	LT05_L2SP_070014_19850831_20200918_02_T1	1985	106	67	-147.8742	64.8962

Finally, the pixel-based SR and LR water classifications were converted to vector objects. First, water pixels were polygonized, and morphological closing (i.e. successive outwards, then inwards buffering) was performed to aggregate adjacent lake fragments. Based on Kyzivat et al. (2019b), a 10 m buffer was used, which aggregated any lake fragments within 20 m of each other. Next, the river mask of Kyzivat et al. (2022) was expanded to cover the remaining regions and used to remove rivers. Finally, lake polygons were clipped to a region of interest (ROI) defined as the intersection of the original Landsat and AirSWOT camera scene boundaries. Any fractional lakes that overlapped scene boundaries or resulted from clipping out the river mask were retained to preserve a large sample size. For consistency, the same river removal and ROI cropping was applied to the GT lake polygons, and the resulting polygons thus included lakes detected in LR, SR and GT, all with a common ROI and a 40 m^2 native MMU.

2.4 Evaluation of lake object detection performance

To assess lake geolocation accuracy, three fine-scale metrics were calculated to compare SR versus LR object detections against GT: precision (true positives as a fraction of total GT lakes), recall (true positives as a fraction of all identified lakes), and F-1 score (a derivative accuracy measure). We consider these metrics fine-scale because they are only computed between two objects at a time. True positives (TPs) were defined as lake objects in SR (or LR) that overlapped or fell within 30 m of a GT lake object. This 30 m tolerance was chosen based on the 30 m Landsat pixel size, the known geolocation accuracies of LR (12 m) and GT (14.7 m), and the expectation that sub-pixel SR lakes would not necessarily overlap GT lakes but should nonetheless count as valid detections if they are located within a small tolerance. Type I error (commission) was assessed through Precision and Type II error (omission) through recall as follows:

$$Precision = \frac{TP}{TP+FP} \qquad [1]$$

$$Recall = \frac{TP}{TP+FN} \qquad [2]$$

where FP are false positives and FN are false negatives. The F-1 score was calculated as the harmonic mean of precision and recall. All three metrics vary from 0 to 1, with 0 indicating no overlap and 1 indicating perfect agreement. To compare LR and SR object detections to GT, they were calculated for all study regions in aggregate.

To find an appropriate MMU to use for error assessment and to reduce uncertainty through averaging, these fine-scale metrics precision, recall, and F-1 score were computed over a variety of distance and size thresholds. First, to find a reliable MMU, a series of truncated datasets were created (referred to as the full GT comparison) by progressively filtering out LR and SR lakes based on 20 logarithmically-spaced minimum sizes ranging from 40 to 10^7 m^2. The fine-scale metrics were computed at each threshold, and since precision and recall were monotonic, F-1 score had a clear maximum and was used to determine the MMU as the lake size threshold that maximized it (**Figure 4a-c**). Next, truncated datasets were again created, except GT lakes were included in the truncation (referred to as the truncated GT comparisons, **Figure 4d-f**). Given this equal truncation of datasets, results could be used to determine classifier performance at the MMU or at any size threshold. Finally, similar to previous studies (Shermeyer et al. 2018; Courtrai et al. 2020), averages of the fine-scale metrics precision, recall, and F-1 score (AP, AR, AF1) were computed over distance tolerances varying from 0 m to 30 m in 5 m increments. These estimates and following summary statistics were computed at the determined MMU for 10x SR, which represents the smallest-sized lake for which errors of commission and omission are balanced.

Lakes vary considerably in size, necessitating scale-independent metrics that can be applied across image tiles to evaluate lake sizes and counts. We modeled the lake-size distribution (LSD, Cael and Seekell 2016, Kyzivat et al. 2019b) as a power law (Clauset et al. 2009, Virkar et al. 2014, Horvat et al. 2019) to test for scale-invariant behavior. A power law distribution has the property of scale invariance (Cael and Seekell 2016) and takes the form:

$$P(a > A) = CA^{-\alpha} \qquad [3]$$

where A is a given lake area, and C and α are fitted constants. The best-fitting power law was obtained using the python *powerlaw* package, which first finds the optimal minimum value A_0 for the onset of power law behavior by minimizing the Kolmogorov–Smirnov distance between the data and fit over potential A_0 values (Alstott et al. 2014). The parameter α is fit for the optimal A_0 using a maximum likelihood estimator, and the Kolmogorov–Smirnov test is subsequently run to find a p-value for a power-law fit compared to the null hypothesis of an exponential distribution. The fitted SR and LR LSDs were evaluated against that of GT based on mean and median lake sizes and fitted power law parameters.

2.5 Retroactive application of SR to a 1985 Landsat 5 image

To assess retroactive application of a Planet-trained SR model to older Landsat imagery, a 31 August 1985 Landsat 5 scene (**Table 1**) was chosen to correspond to an air photo-derived lake shoreline dataset for Fairbanks, AK, USA from 23 December of the same year (Walter Anthony and Lindgren 2021). Like the contemporary GT dataset, lake shorelines in this historical GT dataset were derived using semi-automated, object-based image classification and were manually edited to remove rivers (Lindgren et al. 2016, 2019). Although this dataset has a minimum lake size of 13 m^2, we truncated it to 40 m^2 for consistency with the modern GT dataset. Identical image processing and statistical analysis, as described in **Sections 2.1-2.4**, were applied to the corresponding Landsat 5 scene, except an ROI was manually drawn to exclude frequently misclassified urban areas surrounding Fairbanks. This processing produced 242 historical GT lakes from the year 1985 ranging from 40 m^2 to 0.10 km^2 in area.

3. Results

3.1 Radiometric consistency

Comparison of SR and LR pixel value frequency distributions reveals a generally good match between LR and SR with no difference in mean band values (**Figure 2**), and image coloration appears unchanged (**Figure 3**). The Wilcoxon signed-rank test showed no statistical difference in mean per band over the 11 scenes (p=0.31), with an anomaly of -4.7, 1.7, and -0.4 DN units compared to LR band means for (N,G and R bands, respectively). Even so, each histogram pair was determined statistically distinct by the highly-sensitive Kolmogorov–Smirnov test (p = 0). Thus, the SR transformation can subtly change the pixel distributions but does not introduce a bias.

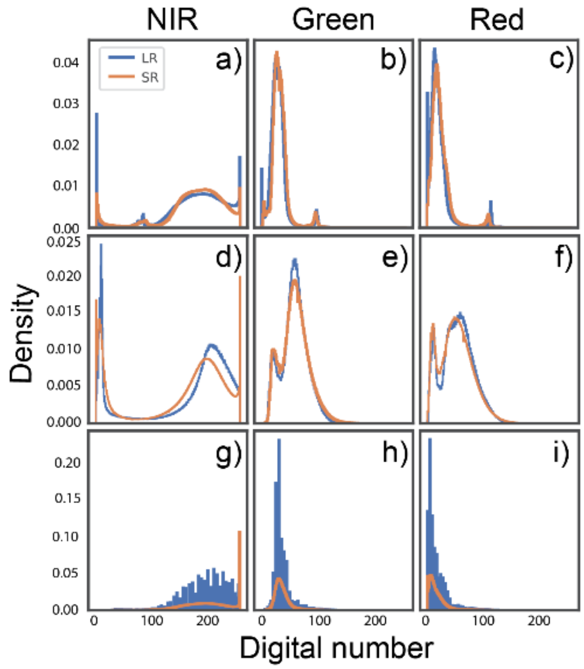

Figure 2. Example pixel frequencies for Yukon Flats, Alaska (**a-c)**, Canadian Shield near Baker Creek (**d-f**), and Fairbanks, AK 1985 (**g-i**). Bin counts are normalized to facilitate comparison between data sets of different sizes. Jagged Landsat 5 histograms are a result of the 1-95% image stretch applied to native 8-bit radiometric resolution. In contrast, the SR transformation produces smooth histograms that make use of the total dynamic range.

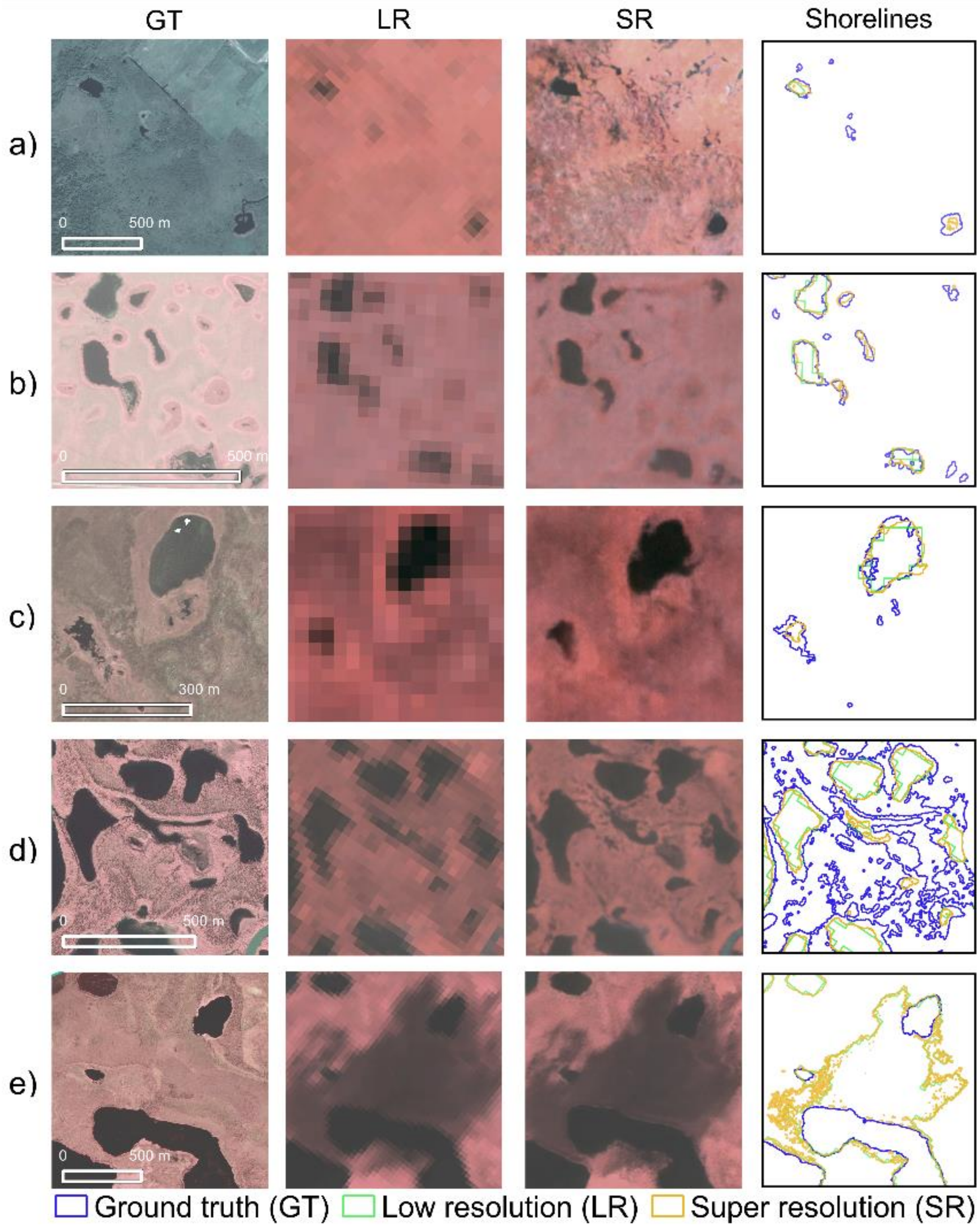

Figure 3. Airborne camera GT and Landsat LR and SR examples demonstrate the advantages of SR in Fairbanks, Alaska, 1985 (**a**); Prairie Potholes South, North Dakota (**b**); and Canadian Shield Margin, Northwest Territories **(c)**. Two examples show instances of classifier error in Mackenzie River Delta, Northwest Territories (**d**); and Old Crow Flats, Yukon territories (**e**). In row **(a)**, an additional lake is detected in SR compared to LR for Landsat 5 data from 1985. In **(b)**, the lake in the northeast corner has a SR lake detection within thirty meters of GT, showing how use of an adjacency buffer better evaluates results. In row **(c)**, SR classification detects one lake missed in LR, but both classifiers miss three lakes sized near the native GT MMU. In row **(d)**, errors in GT classification caused by tree shadows produce apparent false negatives in the SR and LR classifications, demonstrating that GT has its own sources of error. A river in the southeast corner is effectively masked out and therefore does not contribute to summary metrics. In row **(e)**, a cloud shadow in the Landsat image causes false positives in SR and LR,

demonstrating errors caused by lack of temporal synchronicity with GT. Center coordinates: 64.8775, -147.7242 (**a**); 47.1432, -99.2494 (**b**); 63.7498, -117.6939 (**c**); 68.2280, -134.5631 (**d**); 47.1543, -99.2204 (**e**).

3.2 Determination of an appropriate minimum mapping unit (MMU) for Landsat SR imagery

An optimal MMU of 500 m^2 was identified for lake detection in Landsat SR imagery and used to compute metrics for both resolutions. From the full GT comparison used for sensitivity analysis, SR F-1 score peaks at this lake size (**Figure 4c**), signifying best tradeoff between type I and II errors for lakes of this size. LR also has a subtle maximum around 40-1,000 m^2, but we do not consider it robust enough to unequivocally state an LR MMU, a task which we defer to previous studies. The observed overall similarity in SR and LR F-1 curves despite a 10x difference in spatial scale suggests that this property is largely independent of pixel size and likely tied to intrinsic sensor resolution. Therefore, from the F-1 score plot (**Figure 4c**), we identify an optimal MMU of 500 m^2 ($^2/_3$ Landsat pixel) for 10x SR lake detection and use this MMU for subsequent metrics for both SR and LR.

3.3 Detection of small lakes in contemporary Landsat SR imagery

SR imagery detects small lakes more reliably than does LR (**Figure 3**). Despite inferior precision for lakes < ~1,000 m^2 (~1 Landsat pixel), the SR classifier yields superior recall and F-1 scores for lakes < 10,000 m^2 (~10 Landsat pixels, **Figure 4a-c**). SR and LR AF1 scores are 0.75 and 0.73, respectively, for lakes larger than the 500 m^2 MMU (**Table 2**). In addition, the area under the precision-recall curve (**Figure 4g**) is greater for SR (0.57) than for LR (0.48), implying improved performance, even when averaged over all 20 minimum lake size thresholds used to compute it. The high precision (low type I error) of LR in detecting small lakes can be attributed to under-sampling of small lakes in the LR dataset. In this size range, only the LR lakes with the darkest NIR values are detected, and as a result, they are unlikely to be false positives. In contrast, SR false positives are more common due to confusion with roads, shadows, and fragments of rivers not included in the river mask. In sum, more small lakes can be detected in SR than in LR imagery, but at the expense of some false detections, leading to modest gains overall.

Table 2. SR lake detections have better skill than LR for lakes larger than 500 m^2, as measured by Average Recall (AR) and F-1 score (AF1), but not by Average Precision (AP), when compared against GT. These averages are derived from the data shown in **Figure 6** for tolerances <= 30m.

		AP	**AR**	**AF1**
Landsat 8	LR	**0.75**	0.71	0.73
	SR	0.74	**0.77**	**0.75**
Landsat 5	LR	**1.00**	0.31	0.47
	SR	0.98	**0.43**	**0.60**

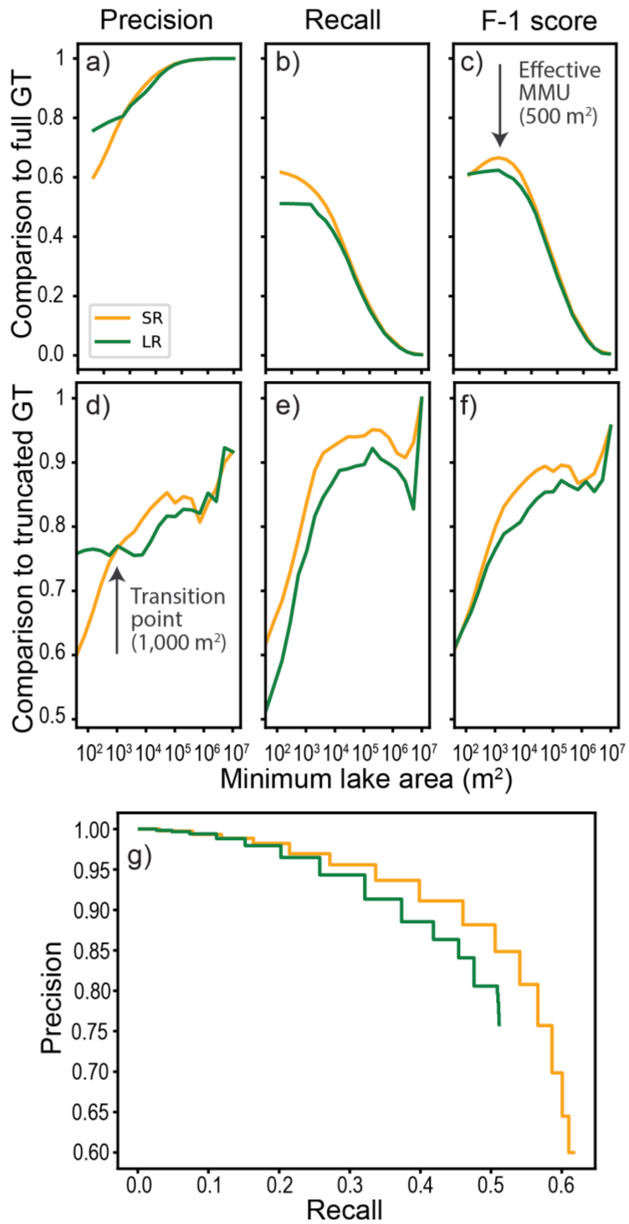

Figure 4. Accuracy metrics for different minimum lake sizes indicate that recall and F-1 scores are greater for Landsat SR than LR for all lake sizes (**e, f**), while precision varies and is less for SR than LR for small lakes until a transition at 1,000 m^2 (**d**). An effective MMU of 500 m^2 ($^2/_3$ of a Landsat pixel) is determined based on the global maximum of F-1 score in **(c)**. Metrics are calculated against all GT lakes (**a-c**), and for GT lakes only above the corresponding lake size threshold (**d-f**), with the latter curves being noisier due to the sample size decreasing with size threshold. The precision-recall curve (**g**) is plotted using data in (**d-f**), and the SR classification has a greater area under the curve (0.57) than that of LR (0.48).

The SR water classification yields a remarkably accurate number and size distribution of lakes if all potential lake detections are included (**Figure 5a**). From 25,281 GT lakes, 25,990 are detected in SR and 17,059 in LR, a 2.8% difference (**Table 3**). The mean and median lake sizes determined from SR agree with GT by +7.7 and +37 %, respectively, representing significant improvements over LR (+72% and +711%, respectively). A lake-size distribution histogram based on only true positives shows improved agreement compared to the LR histogram, especially for smaller lake sizes (**Figure 5b**). It is evident that many of these correctly sized lakes are located outside of the 30 m tolerance used to define a true positive. For lakes larger than the 500 m^2 MMU, the classifier obtains a 78.1% recall over all remaining size bins (**Figure 4e**). If this tolerance is relaxed to 90 m, the recall for SR increases to 83.8%, signifying that about $^1/_3$ of these false positive lakes are "near misses" within 90 m (**Figure 6b**). Overall, SR lakes show good agreement with GT in number and size, representing significant improvements over LR.

Table 3. Scale-independent lake detection metrics of count (N), true positives, lake area, and power law parameters A_0 (optimal onset of power law behavior) and α (fitted power law slope). All reported α and A_0 values have statistical significance at a 0.001 significance level. SR outperforms LR in estimating the count and mean and median lake size, and pixel resolution has no effect on estimating the power law exponent α, or the onset of power-law behavior A_0.

Resolution	N	N (greater than MMU)	True positives	Mean lake area (m^2)	Median lake area (m^2)	α	A_0 (m^2)
GT	25,281	14,522	-	54,639	899	2.151 ± 0.061	536,738
LR	17,059	15,226	10,533	93,988	7,288	2.197 ± 0.056	471,756
SR	25,990	13,947	11,339	58,835	1,235	2.194 ± 0.069	698,115
GT*	43,562	23,178	-	137,000	665	1.89 ± 0.04	343,074

*A comparison is made to Kyzivat et al. (2019b), which uses a similar domain to GT, but includes large lakes not completely observable by the narrow airborne swaths used here.

Power-law LSD behavior is evident for larger lakes at all three resolutions, as indicated by a constant slope when plotted as a survival function in log-log space (**Figure 5e**). Fitted truncated power laws (Clauset et al. 2009) show no significant difference in the power law exponent or minimum size parameters (**Table 3**). Even so, the SR LSD is a better approximation than the LR LSD, which has a power law slope matching GT for the large lakes where it can be computed, but exhibits slope deviations for small lakes (**Figure 5e**). Thus, the SR-derived LSD closely matches the GT LSD, offering significant improvement over the LR-derived LSD.

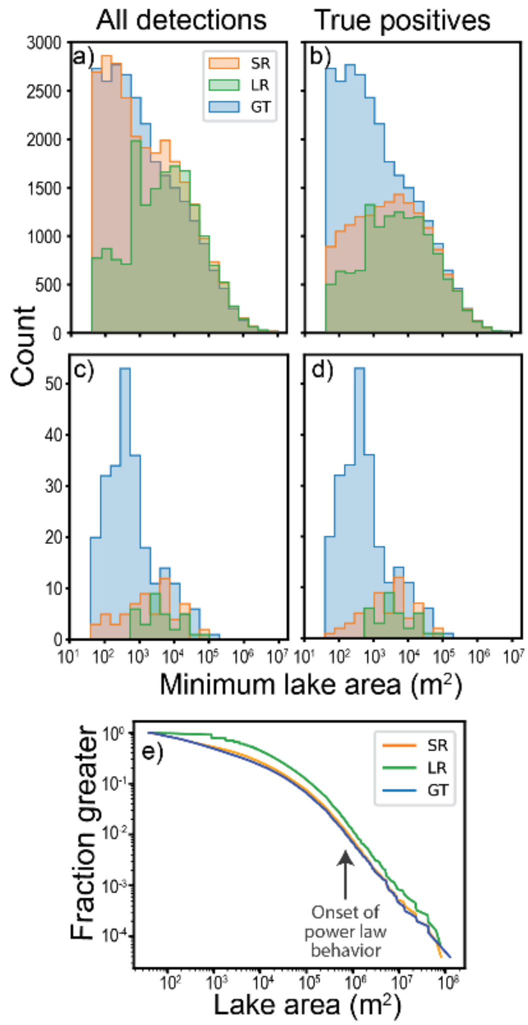

Figure 5. Lake-size distribution histograms based on all detected lakes (**a, c**) show good agreement between the size frequencies of SR and GT lakes for contemporary Landsat 8 scenes (**a, b**) and historical Landsat 5 scenes (**c, d**). When only plotting true positive lakes, this agreement is diminished, although SR still detects more lakes than LR in nearly all size bins up to 10,000 m^2 for both recent (**b**) and 1985 (**d**) Landsat imagery. Removing rivers occasionally led to LR lakes counterintuitively smaller than one 900 m^2 Landsat pixel (**a, b**). These lakes were nevertheless retained to follow consistent geoprocessing steps for all datasets.

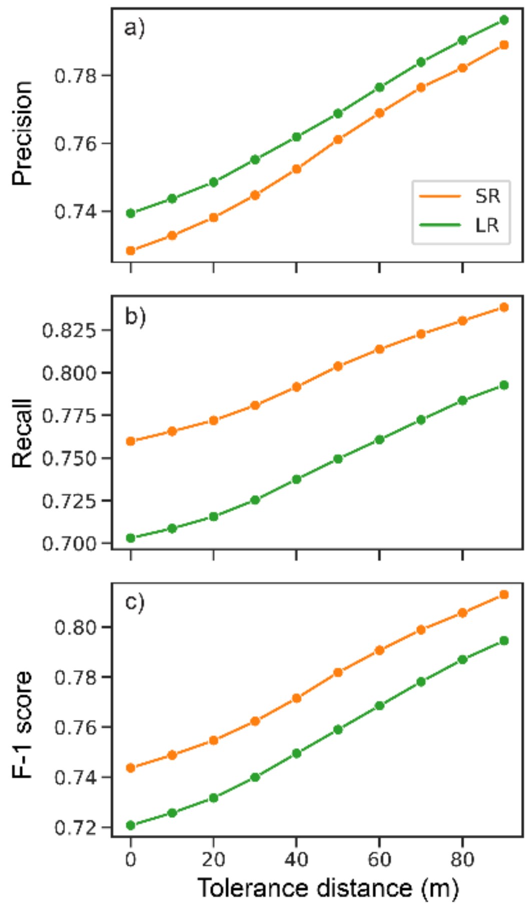

Figure 6. Accuracy metrics for different tolerance distances to 90 m based on the assumed MMU of 500 m^2.

3.4 Detection of small lakes in historical Landsat SR imagery

SR lake detection was also successfully demonstrated for a 1985 Landsat 5 scene over Fairbanks, Alaska, USA. Like with Landsat 8, SR lake detections have inferior precision, but superior recall and F-1 scores compared to LR lake detections (**Table 2**). Compared with Landsat 8 statistics, the 1985 Landsat 5 SR scene yields superior precision (AP=0.98 for Landsat 5, vs. 0.75 for Landsat 8) but inferior recall (AR= 0.43 vs. 0.77) and F-1 score (AF1= 0.60 vs. 0.75) (**Table 2**). Notably, SR lake detection yields only one false positive in this scene, and LR yields none, producing higher AP values than the Landsat 8 scenes. The low AR and AF1 values are likely due to the finer native resolution of the historic Fairbanks shoreline dataset (minimum lake size of 13 m^2, Lindgren et al. 2016) than the contemporary GT dataset (40 m^2 minimum, Kyzivat et al. 2018), even though both were ultimately truncated to 40 m^2 for plotting and to 500 m^2 for summary metrics. Since the historical GT dataset has higher native resolution than the contemporary GT dataset, these differences in AR and AF1 are likely a product of GT dataset comprehensiveness, not of Landsat sensor properties.

4. Discussion

4.1 Significance of results

Here, we demonstrate that a 3 m SR model trained solely on Planet SmallSat imagery can be used to super-resolve 30 m contemporary and historical Landsat imagery to detect small Arctic-boreal lakes at sub- to several-pixel scales. Our cross-sensor application of SR to lake mapping is an advance over previous practices in at least three ways: 1) it quantifies an SR MMU for lake object detection; 2) it assesses error using fine-scale and scale-independent object-based metrics; and 3) most significantly, it shows that a model trained by degrading HR imagery to obtain LR (here, 3 m resolution Planet SmallSat imagery, degraded to 30 m) can be successfully applied to a different LR instrument (here, contemporary and historical 30 m Landsat imagery). Because our approach performs cross-sensor training using only one sensor (i.e. Planet), this advance is of particular value to the Landsat archive, which long predates widely-available high-resolution imagery.

Our results suggest that Landsat 10x SR provides little improvement to precise geolocational mapping of small lakes, yet some improvement to overall lake detection. Gains caused by improved spatial resolution are offset by increases in false positive detections, of which ~$^1/_3$ are "near misses" (i.e. 35% are located within 30-90 m of real-world lake, **Section 3.3**). Despite these geolocational errors, improvements in overall lake detection (**Table 2**) are evident, depending on which metric and error types are considered. Our observed reduction in AP caused by SR is on par with the outer range of Shermeyer et al. (2018), who found typical mean average precision (mAP, a multi-class analog to AP) ranging from 0.55 to 0.59, representing an increase in mAP of -0.2 to 0.11 compared to LR object detection for various resampling ratios. The 8x SR model of Courtrai et al. (2020) had an AP of 0.55 to 0.77 and an F-1 score of 0.03 to 0.86, with no available GT at that resolution for comparison. Our contemporary Landsat AP of 0.75 (LR) and 0.74 (SR) (**Table 2**) falls within the range of these two previous studies, both in magnitude and in lack of SR performance gain. In both studies, the objects being detected were larger than ~5 LR pixels, with objects in Shermeyer et al. (2018) typically between 10 and 50 pixels. In contrast, our smallest detectable lakes are of subpixel size, which explains why SR produces a decrease in AP in our study, while this was a rare occurrence for Shermeyer et al. (2018). Neither of these studies report AR, which measures type II error and can be just as important as type I error, depending on the application (Matsuda et al. 2006). Based on AR and AF1, we show incremental improvement in SR lake detection with our suggested MMU of 500 m^2 offering the best tradeoff between type I and II error.

Our quantification of cross sensor performance using scale-independent metrics, such as the lake-size distribution (LSD), offers additional scientific benefits beyond Landsat SR performance assessment. In particular, SR imagery can help determine whether observed slope breaks in LSD plots are due to sensor resolution or to a physical process in lake formation. Using airborne camera imagery Kyzivat et al. (2019b) find an onset of power law behavior at 343,074 m^2, which is in general agreement with our results of 536,738 to 698,115 m^2 (**Table 3**). This size limit is within the range of MMUs of 3,600 m^2 – 30,000 m^2 (4-33 pixels) from previous studies (Pekel et al. 2016, Kyzivat et al. 2019b; Muster et al 2019; Sui et al. 2022; Verpoorter et al. 2014; Paltan et al. 2015; Pi et al. 2022) and well above our own recommendation of $^2/_3$ of a pixel for SR Landsat imagery. This high size limit indicates that the onset of power law behavior is a true geophysical phenomenon, not an artifact of sensor resolution. Thus, scale-based lake estimates cannot be improved by increasing spatial resolution, and SR is better used for direct lake counting.

The main value added by applying an SR model to Landsat imagery is improved lake counts and size distributions, particularly for small lakes sized around one to several pixels. For example, even when truncating all datasets to 40 m^2, our LR classifier still detects fewer lakes than both GT and SR, particularly for small lakes up to 8,000 m^2 or 11,000 m^2 (~9-12 pixels) depending on whether false positives are included (**Figure 5a**) or excluded (**Figure 5b**). Clearly, our LR classifier under-counts lakes smaller than the conventionally-used LR Landsat MMU (3,600 – 30,000 m^2 or ~4-33 pixels, **Section 1**). SR thus offers a remedy for this under-counting by decreasing the reliable MMU for LR imagery and yielding unbiased estimates of lake count. Although not always improving geolocational accuracy, SR can be used for estimating the overall bulk size distribution and abundance of Arctic-boreal lakes.

The most promising aspect of our cross-sensor SR study its successful application to historical Landsat 5 imagery (**Figure 2**, **Figure 3**, **Table 1**). We show that this application yields improved detection of small lakes based on a threshold-based image classification (**Figure 4**, **Table 2**). To our knowledge, no historical object detection from SR has been previously shown or evaluated). The SR transformation produces a small but statistically insignificant bias in radiometric values, consistent with Lezine et al. (2021), who showed a negative or zero pixel value bias, and with Salgueiro Romero et al. (2020) whose cross-sensor SR model showed little change in image histogram shape. Thus, the SR transformation from ESRGAN (and perhaps other) models appears to have little impact on image radiometric properties, even across sensors. Importantly, unlike Salgueiro Romero et al. (2020) and other cross-sensor SR studies (Galar et al. 2020; Yoo et al. 2021), our model was trained with imagery derived from only one sensor (Planet), yet could still be transferred to another sensor (Landsat), opening up the possibility of further retroactive generation of SR.

4.2 Ethical considerations of super resolution object detection

Our retroactive generation of super resolution (SR) imagery for a time when no satellite high resolution (HR) imagery was publicly available raises interesting ethical concerns about the production and use of satellite SR imagery. First, there is a human proclivity to regard image data, particularly from high-resolution satellite images, as accurate, neutral or politically uncharged (Bennett et al. 2022). This proclivity is concerning when considering that satellite SR images are commonly derived from GANs, models originally designed to create synthetic, or fake, data (Goodfellow et al. 2014). A known byproduct of ESRGAN (Wu et al. 2018) and other GAN-based models (Wang et al. 2022), for example, is their tendency to produce spurious but seemingly realistic image features (e.g. Lezine et al. 2021). GANs and other artificial intelligence models used in earth observation also suffer from a lack of explainability (Gevaert 2022), which can make users less likely to evaluate their uncertainties. While the ethical consequences of misplaced Arctic-boreal lakes shown here are innocuous, both type I and type II errors in other applications of SR object detection, such as intelligence gathering (e.g. Shermeyer et al. 2018) could have serious ramifications. A related concern is the deliberate use of SR satellite images to mislead or disseminate disinformation, for example, with deep fakes (Xu et al. 2018, Zhao et al. 2021). Put simply, there is an innate allure to high spatial resolution imagery that human interpreters should be cognizant of when viewing retroactive SR satellite products for which no independent high-resolution information is available for verification. We therefore caution that the approach presented here may safely be applied to assess bulk lake count inventories and size distributions (LSDs), but not to determine specific geolocational positions or areas of individual lakes.

4.3 Limitations and future work

Small lakes are more readily detected in SR than in LR imagery, but at the expense of more false detections. To balance these effects and increase reliability, we suggest considering only those objects larger than our suggested 10x Landsat SR MMU. Given an MMU of ~ $^2/_3$ of Landsat pixel, 10x super resolution appears to be an unnecessarily high resolution ratio for hydrological mapping, and 2x or 4x ratios may be just as effective. Future work could quantify the gain in intrinsic spatial resolution of SR images (Valenzuela et al. 2022) in comparison to the nominal resolution ratio. Results could also be improved by incorporating multi-temporal inputs using techniques from multi-image or video SR (Xiao et al. 2022). While we here degraded the radiometric resolution of Landsat-8 to 8-bit data, future investigations should make full use of the native 16-bit radiometric resolution of Landsat 7-9 for contemporary SR studies. Our GT dataset derived from narrow airborne flight lines cannot detect large lakes in their entirety, and we made no attempt to correct for associated impacts on LSD (Kyzivat et al. 2019b) or to improve the realism of lake shapes (Muad and Foody 2011). This study's first demonstration for a single Landsat 5 SR image leaves abundant opportunities for future studies comparing larger Landsat 5 datasets with historical air photos, maps, or other fine-scale information. Finally, we note a dearth of ethics studies examining the creation, use, and dissemination of SR satellite imagery, and hope our brief discussion prompts future work in this area.

5 Conclusion

We demonstrate generation of 3 m super resolution (SR) imagery from archived 30 m Landsat imagery, using a general adversarial network (GAN) trained entirely with independent, high-resolution Planet SmallSat imagery. This cross-sensor generation of SR is unique in not requiring time-intensive image cross-normalization techniques, and in seeking to detect small objects (lakes) at sub- to several-pixel scales. Furthermore, we show the reliable detection of lakes in Landsat 5 and 8 imagery as small as ~$^{2}/_{3}$ of a Landsat pixel (500 m^2), a significant improvement over the 4-33 pixel limit typically used for native resolution Landsat imagery. The super-resolved 3 m resolution of Landsat SR imagery does not adversely impact radiometric values, introducing only a small, statistically insignificant bias. Total SR lake counts agree within a remarkable +2.8% of ground truth (GT) if false positives are allowed and -55% if they are excluded. In contrast, total lake counts from native-resolution (30 m) Landsat imagery agree within -32%, and -58%, respectively. Compared to unenhanced imagery, a SR transformation improves the type II error (recall) and F1-score of lake detection, but not the type I error (precision) for both Landsat 5 (1985) and 8 (2017). Type II error has been largely overlooked by previous studies but is more relevant than type I error for assessing lake abundance. From this early demonstration, we conclude that classifications of cross-sensor SR improves estimates of the overall abundance and size distribution of lakes, and that onset of power law behavior in lake size distributions (LSDs) is a true geophysical phenomenon, not an artifact of sensor resolution. Even so, SR-derived lake maps contain "realistic-looking" errors in lake geolocation and shoreline details. They should thus be interpreted with caution and are best used for bulk estimation of total lake abundance and LSD. Much work remains surrounding the creation of SR models, their retroactive application to historical satellite imagery, and formulation of ethical guidelines for the production, interpretation, and use of SR images.

Acknowledgements

The authors would like to thank Ekaterina Lezine and Prof. Karianne Bergen for helpful guidance.

Funding

This work was funded by the Future Investigators in NASA Earth and Space Science and Technology (FINESST) fellowship managed by Dr. Allison Leidner (grant number 80NSSC19K1361) and the NASA Terrestrial Hydrology Program (grant number 80NSSC20K0429) managed by Dr. Jared Entin.

Availability of data and code

Code and data used for this analysis are available on GitHub (https://github.com/ekcomputer/pixel-smasher) and Zenodo (https://doi.org/10.5281/zenodo.7306219).

Competing interests

The authors declare no competing interests.

REFERENCES

Eirikur Agustsson, & Radu Timofte. (2017). NTIRE 2017 challenge on single image super-resolution: Dataset and study. *IEEE Computer Society Conference on Computer Vision and Pattern Recognition Workshops*, *2017-July*, 1122–1131. https://doi.org/10.1109/CVPRW.2017.150

Allen, G. H., Pavelsky, T. M., Barefoot, E. A., Lamb, M. P., Butman, D., Arik Tashie, & Gleason, C. J. (2018). Similarity of stream width distributions across headwater systems. *Nature Communications*, *9*(1), 610. https://doi.org/10.1038/s41467-018-02991-w

Alstott, J., Bullmore, E., & Dietmar Plenz. (2013). *Powerlaw: a Python package for analysis of heavy-tailed distributions*. https://doi.org/10.1371/journal.pone.0085777

Anthony, K.W., and P. Lindgren. 2021. ABoVE: Historical Lake Shorelines and Areas near Fairbanks, Alaska, 1949-2009. ORNL DAAC, Oak Ridge, Tennessee, USA. https://doi.org/10.3334/ORNLDAAC/1859

Anthony, W., Lindgren, P., Hanke, P., Engram, M., Anthony, P., Daanen, R. P., Bondurant, A., Liljedahl, A. K., Lenz, J., Grosse, G., Jones, B. M., Brosius, L., James, S. R., Minsley, B. J., Pastick, N. J., Munk, J., Chanton, J. P., Miller, C. E., & Meyer, F. J. (2021). Decadal-scale hotspot methane ebullition within lakes following abrupt permafrost thaw. *Environ. Res. Lett*, *16*, 35010. https://doi.org/10.1088/1748-9326/abc848

Bennett, M. M., Chen, J. K., Alvarez, L. F., & Gleason, C. J. (2022). The politics of pixels: A review and agenda for critical remote sensing. *Progress in Human Geography*, *46*(3), 729–752. https://doi.org/10.1177/03091325221074691

Cael, B. B., & Seekell, D. A. (2016). The size-distribution of Earth's lakes. *Scientific Reports*, *6*(29633). https://doi.org/10.1038/srep29633

Clauset, A., Cosma Rohilla Shalizi, & Newman, M. E. J. (2009). Power-law distributions in empirical data. *SIAM Review*, *51*(4), 661–703. https://doi.org/10.1137/070710111

Downing, J. A., Prairie, Y. T., Cole, J. J., Duarte, C. M., Tranvik, L. J., Striegl, R. G., McDowell, W. H., P. Kortelainen, Caraco, N. F., Melack, J. M., & Middelburg, J. J. (2006). The global abundance and size distribution of lakes, ponds, and impoundments. *Limnology and Oceanography*, *51*(5), 2388–2397. https://doi.org/10.4319/lo.2006.51.5.2388

Fayne, J. V., Smith, L. C., Pitcher, L. H., E.D. Kyzivat, Cooley, S. W., Cooper, M. G., M.W. Denbina, Chen, A. C., Chen, C. W., & T.M. Pavelsky. (2020). Airborne observations of arctic-boreal water surface elevations from AirSWOT Ka-Band InSAR and LVIS LiDAR. *Environmental Research Letters*, *15*(10). https://doi.org/10.1088/1748-9326/abadcc

Fernando, L., Marcello, J., & Verónica Vilaplana. (2020). Super-resolution of Sentinel-2 imagery using generative adversarial networks. *Remote Sensing*, *12*(15), 2424. https://doi.org/10.3390/RS12152424

Galar, M., Sesma, R., Ayala, C., Albizua, L., & Aranda, C. (2020). Super-resolution of sentinel-2 images using convolutional neural networks and real ground truth data. *Remote Sensing*, *12*(18), 2941. https://doi.org/10.3390/rs12182941

Gevaert, C. M. (2022). Explainable AI for earth observation: A review including societal and regulatory perspectives. *International Journal of Applied Earth Observation and Geoinformation*, *112*, 102869. https://doi.org/10.1016/J.JAG.2022.102869

GDAL/OGR contributors. (2022). *GDAL/OGR geospatial data abstraction software library*. https://doi.org/10.5281/zenodo.5884351

Goodfellow, I. J., Pouget-Abadie, J., Mirza, M., Xu, B., Warde-Farley, D., Sherjil Ozair, Courville, A., & Yoshua Bengio. (2014, June). *Generative adversarial networks*. Advances in Neural Information Processing Systems. http://arxiv.org/abs/1406.2661

Harris, C. R., K. Jarrod Millman, van, Ralf Gommers, Pauli Virtanen, Cournapeau, D., Wieser, E., Taylor, J., Berg, S., Smith, N. J., Kern, R., Matti Picus, Hoyer, S., Kerkwijk, Brett, M., Haldane, A., Fernández, J., Wiebe, M., Peterson, P., & Gérard-Marchant, P. (2020). Array programming with NumPy. *Nature 2020 585:7825*, *585*(7825), 357–362. https://doi.org/10.1038/s41586-020-2649-2

Horvat, C., Roach, L. A., Tilling, R., Bitz, C. M., Baylor Fox-Kemper, Guider, C., Hill, K., Ridout, A., & Shepherd, A. (2019). Estimating the sea ice floe size distribution using satellite altimetry: Theory, climatology, and model comparison. *Cryosphere*, *13*(11), 2869–2885. https://doi.org/10.5194/TC-13-2869-2019

Ignatov, A., Radu Timofte, Thang Van Vu, Tung Minh Luu, Pham, T. X., Cao Van Nguyen, Kim, Y., Jae Seok Choi, Kim, M., Huang, J., Ran, J., Xing, C., Zhou, X., Zhu, P., Geng, M., Li, Y., Eirikur Agustsson, Gu, S., Luc Van Gool, & Etienne de Stoutz. (2019). PIRM challenge on perceptual image enhancement on smartphones: Report. *Lecture Notes in Computer Science (Including Subseries Lecture Notes in Artificial Intelligence and Lecture Notes in Bioinformatics)*, *11133 LNCS*, 315–333. https://doi.org/10.1007/978-3-030-11021-5_20/FIGURES/13

Kyzivat, E. D., Smith, L. C., Fenix Garcia-Tigreros, Huang, C., Wang, C., Langhorst, T., Fayne, J. V., Harlan, M. E., Yuta Ishitsuka, Feng, D., Dolan, W., Pitcher, L. H., Wickland, K. P., Dornblaser, M. M., Striegl, R. G., Pavelsky, T. M., Butman, D. E., & Gleason, C. J. (2022). The importance of lake emergent aquatic vegetation for estimating arctic-boreal methane emissions. *Journal of Geophysical Research: Biogeosciences*, *127*(6), e2021JG006635. https://doi.org/10.1029/2021JG006635

Kyzivat, E.D., L.C. Smith, L.H. Pitcher, J. Arvesen, T.M. Pavelsky, S.W. Cooley, and S. Topp. 2018. ABoVE: AirSWOT Color-Infrared Imagery Over Alaska and Canada, 2017. ORNL DAAC, Oak Ridge, Tennessee, USA. https://doi.org/10.3334/ORNLDAAC/1643

Kyzivat, E.D., L.C. Smith, L.H. Pitcher, J.V. Fayne, S.W. Cooley, M.G. Cooper, S. Topp, T. Langhorst, M.E. Harlan, C.J. Gleason, and T.M. Pavelsky. 2019a. ABoVE: AirSWOT Water Masks from Color-Infrared Imagery over Alaska and Canada, 2017. ORNL DAAC, Oak Ridge, Tennessee, USA. https://doi.org/10.3334/ORNLDAAC/1707

Kyzivat, E. D., Smith, L. C., Pitcher, L. H., Fayne, J. V., Cooley, S. W., Cooper, M. G., Topp, S. N., Langhorst, T., Harlan, M. E., Horvat, C., Gleason, C. J., & Pavelsky, T. M. (2019b). A high-resolution airborne color-infrared camera water mask for the NASA ABoVE campaign. *Remote Sensing*, *11*(18), 2163. https://doi.org/10.3390/rs11182163

Ekaterina Lezine, & Kyzivat, E. (2020). *4x and 10x super resolution generator models trained with planet CubeSat satellite imagery*. https://doi.org/10.5281/ZENODO.4171628

Ekaterina M. D. Lezine, Kyzivat, E. D., & Smith, L. C. (2021). Super-resolution surface water mapping on the canadian shield using planet CubeSat images and a generative adversarial network. *Canadian Journal of Remote Sensing*, *47*(2), 261–275. https://doi.org/10.1080/07038992.2021.1924646

Lindgren, P. R., Grosse, G., Anthony, W., & Meyer, F. J. (2016). Detection and spatiotemporal analysis of methane ebullition on thermokarst lake ice using high-resolution optical aerial imagery. *Biogeosciences*, *13*(1), 27–44. https://doi.org/10.5194/BG-13-27-2016

Lindgren, P., Grosse, G., Meyer, F., & Anthony, K. (2019). An object-based classification method to detect methane ebullition bubbles in early winter lake ice. *Remote Sensing*, *11*(7), 822. https://doi.org/10.3390/rs11070822

Luc Courtrai, Pham, M.-T., & Sébastien Lefèvre. (2020). Small object detection in remote sensing images based on super-resolution with auxiliary generative adversarial networks. *Remote Sensing*, *12*(19), 3152. https://doi.org/10.3390/rs12193152

Mathis Loïc Messager, Lehner, B., Grill, G., Nedeva, I., & Schmitt, O. (2016). Estimating the volume and age of water stored in global lakes using a geo-statistical approach. *Nature Communications*, *7*, 1–11. https://doi.org/10.1038/ncomms13603

Matsuda, H. (2005). The importance of type II error and falsifiability. *Human and Ecological Risk Assessment: An International Journal*, *11*(1), 189–200. https://doi.org/10.1080/10807030590920015

Miller, C., Griffith, C. P., Goetz, S. J., Hoy, E. E., Pinto, N., McCubbin, I. B., Thorpe, A. K., M Hofton, Hodkinson, D., Hansen, C., Woods, J., Larson, E., Kasischke, E. S., & Margolis, H. A. (2019). An overview of ABoVE airborne campaign data acquisitions and science opportunities. *Environmental Research Letters*, *14*(8). https://doi.org/10.1088/1748-9326/ab0d44

Muad, A. M., & Foody, G. M. (2012). Super-resolution mapping of lakes from imagery with a coarse spatial and fine temporal resolution. *International Journal of Applied Earth Observation and Geoinformation*, *15*(1), 79–91. https://doi.org/10.1016/J.JAG.2011.06.002

Muster, S., Riley, W. J., Roth, K., Langer, M., Fabio Cresto Aleina, Koven, C. D., Lange, S., Bartsch, A., Grosse, G., Wilson, C. J., Jones, B. M., & Boike, J. (2019). Size distributions of arctic waterbodies reveal consistent relations in their statistical moments in space and time. *Frontiers in Earth Science*, *7*(5). https://doi.org/10.3389/feart.2019.00005

Homero Paltan, Dash, J., & Edwards, M. (2015). A refined mapping of Arctic lakes using Landsat imagery. *International Journal of Remote Sensing*, *36*(23), 5970–5982. https://doi.org/10.1080/01431161.2015.1110263

Pekel, J.-F., Cottam, A., Gorelick, N., & Belward, A. S. (2016). High-resolution mapping of global surface water and its long-term changes. *Nature*, *540*(December), 418–436. https://doi.org/10.1038/nature20584

Pi, X., Luo, Q., Feng, L., Xu, Y., Tang, J., Liang, X., Ma, E., Cheng, R., Rasmus Fensholt, Brandt, M., Cai, X., Gibson, L., Liu, J., Zheng, C., Li, W., & Bryan, B. A. (2022). Mapping global lake dynamics reveals the emerging roles of small lakes. *Nature Communications 2022 13:1*, *13*(1), 1–12. https://doi.org/10.1038/s41467-022-33239-3

Jakaria Rabbi, Ray, N., Schubert, M., Chowdhury, S., & Chao, D. (2020). Small-object detection in remote sensing images with end-to-end edge-enhanced GAN and object detector network. *Remote Sensing*, *12*(9), 1432. https://doi.org/10.3390/rs12091432

Rika Sustika, Andriyan Bayu Suksmono, Danudirdjo, D., & Ketut Wikantika. (2020). Generative adversarial network with residual dense generator for remote sensing image super resolution. *Proceeding - 2020 International Conference on Radar, Antenna, Microwave, Electronics and Telecommunications, ICRAMET 2020*, 34–39. https://doi.org/10.1109/ICRAMET51080.2020.9298648

Shermeyer, J., & Adam Van Etten. (2018, December). *The effects of super-resolution on object detection performance in satellite imagery*. http://arxiv.org/abs/1812.04098

Smith, L. C. (1997). Satellite remote sensing of river inundation area, stage, and discharge: a review. *Hydrol. Process*, *11*, 1427–1439.

Sui, Y., Feng, M., Wang, C., & Li, X. (2022). A high-resolution inland surface water body dataset for the tundra and boreal forests of North America. *Earth System Science Data*, *14*(7), 3349–3363. https://doi.org/10.5194/ESSD-14-3349-2022

Valenzuela, A., Reinke, K., & Jones, S. (2022). A new metric for the assessment of spatial resolution in satellite imagers. *International Journal of Applied Earth Observation and Geoinformation*, *114*, 103051. https://doi.org/10.1016/J.JAG.2022.103051

Verpoorter, C., Tiit Kutser, Seekell, D. A., & Tranvik, L. J. (2014). A global inventory of lakes based on high-resolution satellite imagery. *Geophysical Research Letters*, *41*(18), 6396–6402. https://doi.org/10.1002/2014GL060641

Pauli Virtanen, Ralf Gommers, Oliphant, T. E., Haberland, M., Reddy, T., Cournapeau, D., Evgeni Burovski, Peterson, P., Weckesser, W., Bright, J., van, Brett, M., Wilson, J., K. Jarrod Millman, Nikolay Mayorov, Andrew R.J. Nelson, Jones, E., Kern, R., Larson, E., & Carey, C. J. (2020). SciPy 1.0: fundamental algorithms for scientific computing in Python. *Nature Methods 2020 17:3*, *17*(3), 261–272. https://doi.org/10.1038/s41592-019-0686-2

Wang, P., Bayram, B., & Elif Sertel. (2022). A comprehensive review on deep learning based remote sensing image super-resolution methods. *Earth-Science Reviews*, *232*, 104110. https://doi.org/10.1016/J.EARSCIREV.2022.104110

Wang, X., Yu, K., Wu, S., Gu, J., Liu, Y., Dong, C., Chen Change Loy, Qiao, Y., & Tang, X. (2018, September). ESRGAN: Enhanced super-resolution generative adversarial networks. *The European Conference on Computer Vision Workshops (ECCVW)*. https://github.com/xinntao/ESRGAN http://arxiv.org/abs/1809.00219

Wulder, M. A., Loveland, T. R., Roy, D. P., Crawford, C. J., Masek, J. G., Woodcock, C. E., Allen, R. G., Anderson, M. C., Belward, A. S., Cohen, W. B., Dwyer, J., Erb, A., Gao, F., Griffiths, P., Helder, D., Hermosilla, T., Hipple, J. D., Hostert, P., M. Joseph Hughes, & Huntington, J. (2019). Current status of Landsat program, science, and applications. *Remote Sensing of Environment*, *225*, 127–147. https://doi.org/10.1016/J.RSE.2019.02.015

Wulder, M. A., White, J. C., Loveland, T. R., Woodcock, C. E., Belward, A. S., Cohen, W. B., Fosnight, E. A., Shaw, J., Masek, J. G., & Roy, D. P. (2016). The global Landsat archive: Status, consolidation, and direction. *Remote Sensing of Environment*, *185*, 271–283. https://doi.org/10.1016/J.RSE.2015.11.032

Xiao, Y., Yuan, Q., He, J., Zhang, Q., Sun, J., Su, X., Wu, J., & Zhang, L. (2022). Space-time super-resolution for satellite video: A joint framework based on multi-scale spatial-temporal transformer. *International Journal of Applied Earth Observation and Geoinformation*, *108*, 102731. https://doi.org/10.1016/J.JAG.2022.102731

Xu, C., & Zhao, B. (2018). Satellite image spoofing: Creating remote sensing dataset with generative adversarial networks (short paper). In S. Winter, A. Griffin, & M. Sester (Eds.), *10th International Conference on Geographic Information Science (GIScience 2018)* (Vol. 114, pp. 67:1–67:6). Schloss Dagstuhl–Leibniz-Zentrum fuer Informatik. https://doi.org/10.4230/LIPIcs.GISCIENCE.2018.67

Xu, S., Mu, X., Chai, D., & Zhang, X. (2018). Remote sensing image scene classification based on generative adversarial networks. *Remote Sensing Letters*, *9*(7), 617–626. https://doi.org/10.1080/2150704X.2018.1453173

Yamano, H., Hiroto Shimazaki, Matsunaga, T., Albon Ishoda, McClennen, C., Hiromune Yokoki, Fujita, K., Osawa, Y., & Hajime Kayanne. (2006). Evaluation of various satellite sensors for waterline extraction in a coral reef environment: Majuro Atoll, Marshall Islands. *Geomorphology*, *82*(3-4), 398–411. https://doi.org/10.1016/J.GEOMORPH.2006.06.003

Yang, K., Smith, L. C., Sole, A., Livingstone, S. J., Cheng, X., Chen, Z., & Li, M. (2019). Supraglacial rivers on the northwest greenland ice sheet, devon ice cap, and barnes ice cap mapped using sentinel-2 imagery. *International Journal of Applied Earth Observation and Geoinformation*, *78*, 1–13. https://doi.org/10.1016/j.jag.2019.01.008

Yang, Y., & Newsam, S. (2010). Bag-of-visual-words and spatial extensions for land-use classification. *International Conference on Advances in Geographic Information Systems*. http://weegee.vision.ucmerced.edu/datasets/landuse.html

Yogesh Virkar, & Clauset, A. (2014). Power-law distributions in binned empirical data. *The Annals of Applied Statistics*, *8*(1), 89–119. https://doi.org/10.1214/13-AOAS710

Yoo, S., Lee, J., Bae, J., Jang, H., & Hong Gyoo Sohn. (2021). Automatic generation of aerial orthoimages using sentinel-2 satellite imagery with a context-based deep learning approach. *Applied Sciences (Switzerland)*, *11*(3), 1–25. https://doi.org/10.3390/app11031089

Zhao, B., Zhang, S., Xu, C., Sun, Y., & Deng, C. (2021). Deep fake geography? When geospatial data encounter Artificial Intelligence. *Cartography and Geographic Information Science*, 1–15. https://doi.org/10.1080/15230406.2021.1910075